INTERNATIONAL JOURNAL FOR NUMERICAL METHODS IN FLUIDS
Int. J. Numer. Meth. Fluids 2003; **41**:447–470 (DOI: 10.1002/fld.441)

An implicit pseudo-spectral multi-domain method for the simulation of incompressible flows

P. Droll[1], M. Schäfer[1,*,†], E. Serre[2] and P. Bontoux[2]

[1]*Department of Numerical Methods in Mechanical Engineering, Darmstadt University of Technology, Petersenstr. 30, D-64287 Darmstadt, Germany*
[2]*Department of Numerical Modelling, LMSNM FRE 2405 CNRS, University Aix-Marseille II, IMT La Jetée Technopôle de Château-Gombert, Rue Frederic-Joliot-Curie 38, 13451 Marseille Cedex 20, France*

SUMMARY

A pseudo-spectral method for the solution of incompressible flow problems based on an iterative solver involving an implicit treatment of linearized convective terms is presented. The method allows the treatment of moderately complex geometries by means of a multi-domain approach and it is able to cope with non-constant fluid properties and non-orthogonal problem domains. In addition, the fully implicit scheme yields improved stability properties as opposed to semi-implicit schemes commonly employed. Key components of the method are a Chebyshev collocation discretization, a special pressure–correction scheme, and a restarted GMRES method with a preconditioner derived from a fast direct solver. The performance of the proposed method is investigated by considering several numerical examples of different complexity, and also includes comparisons to alternative solution approaches based on finite-volume discretizations. Copyright © 2003 John Wiley & Sons, Ltd.

KEY WORDS: incompressible flows; spectral methods; domain decomposition

1. INTRODUCTION

Among the various numerical methods developed for the solution of multi-dimensional and time-dependent incompressible flow problems, spectral methods are characterized by an outstanding numerical accuracy. For problems in simple geometries, with this kind of methods a high numerical efficiency can be achieved by employing solvers based on the fast Fourier transformation (FFT) and fast direct Helmholtz solvers within optimized pressure–correction schemes (e.g. Reference [1]). In such situations highly accurate predictions of complex flows

* Correspondence to: M. Schäfer, Department of Numerical Methods in Mechanical Engineering, Darmstadt University of Technology, Petersenstr. 30, D-64287 Darmstadt, Germany.
† E-mail: schaefer@fnb.tu-darmstadt.de

Contract/grant sponsor: Deutsche Forschungsgemeinschaft (DFG)
Contract/grant sponsor: Centre Nationale de la Recherche Scientifique (CNRS)
Contract/grant sponsor: CNRS network of CFD
Contract/grant sponsor: The French-German PROCOPE programme

Received August 2001
Revised 24 June 2002

become possible (e.g. Reference [2]). However, when the problem geometry has a more complex shape, the corresponding schemes severely suffer from the inflexibility of the Helmholtz solver and lose their efficiency. In addition, the efficient application of these methods requires an explicit treatment of convective terms, what may result in restrictive limitations of the time-step size which in turn lead to a poor computational performance for convection-dominated problems.

To save the situation, Guillard *et al.* [3] and Dimitropoulos *et al.* [4, 5] proposed an alternative approach based on the idea of using a kind of Helmholtz solver as a preconditioner within an outer iterative scheme. On the one hand, this allows for non-constant coefficients in the corresponding discrete equations and, therefore, an implicit treatment of convective terms, varying material properties, and non-orthogonal geometries become possible. On the other hand, the special structure of the discrete equations can still be exploited to ensure a high computational efficiency. The approach presented here closely follows these ideas.

For a further enlargement of the geometrical flexibility of spectral methods a variety of authors have considered domain decomposition techniques allowing for the treatment of multi-block geometries (e.g. References [6–9]). Here, we consider a multi-domain technique, which follows the domain decomposition approach developed by Bramble *et al.* [10–12] in a finite-element context.

The capabilities of the proposed method can be summarized as follows:

- spectral accuracy,
- multi-block geometries,
- implicit treatment of diffusive *and* convective terms,
- non-constant fluid properties,
- non-orthogonal flow domains.

While approaches allowing for individual features from the above list are already available in the literature, to the author's best knowledge the present contribution is the first attempt to combine them in an integrated approach making spectral methods applicable to an enlarged class of practical flow problems.

The numerical techniques employed to attain the aforementioned functionality comprise the following approaches:

- a Chebyshev collocation method for spectral spatial discretization,
- an implicit second-order backward differencing scheme for time discretization,
- a domain decomposition technique for handling multi-block geometries,
- a predictor–corrector pressure–correction scheme for coupling of velocity and pressure,
- a preconditioned restarted GMRES solver as outer iteration scheme for linear system solving,
- a preconditioner based on a modified fast direct Helmholtz solver with multi-domain extensions.

It is worth mentioning that the method is also well suited for a parallelization on the basis of the domain decomposition technique. This matter, however, will not be discussed here further. Also, in order to focus our considerations, we will not address the issues of non-constant fluid properties and non-orthogonal flow domains in this paper. Due to the possibility of coping with non-constant coefficients in the differential equations, these can be handled in a straightforward manner.

After outlining the various components of the proposed method, it is investigated with respect to its functionality and computational performance by a variety of numerical test cases. This also includes studies concerning the influence of numerical parameters as well as comparisons to alternative approaches involving standard finite-volume discretizations.

2. GOVERNING EQUATIONS AND BASIC SOLUTION ALGORITHM

In this section the governing equations are formulated, the basic spatial and temporal discretization techniques are summarized, and the underlying iterative pressure–correction scheme for the solution of the coupled discrete non-linear system is outlined.

2.1. Governing equations

We consider the flow of an incompressible Newtonian fluid, for which the basic conservation equations governing transport of mass, momentum and a scalar quantity are given in conservative form by

$$\frac{\partial u_j}{\partial x_j} = 0 \tag{1}$$

$$\frac{\partial(\rho u_i)}{\partial t} + \frac{\partial(\rho u_j u_i)}{\partial x_j} - \frac{\partial}{\partial x_j}\left[\mu\left(\frac{\partial u_i}{\partial x_j} + \frac{\partial u_j}{\partial x_i}\right)\right] = -\frac{\partial p}{\partial x_i} + \rho f_i \tag{2}$$

$$\frac{\partial(\rho s)}{\partial t} + \frac{\partial(\rho u_j s)}{\partial x_j} - \frac{\partial}{\partial x_j}\left(\alpha \frac{\partial s}{\partial x_j}\right) = \rho g \tag{3}$$

where u_i is the velocity vector with respect to Cartesian co-ordinates x_i, t is the time, ρ is the fluid density, μ is the dynamic viscosity, p is the pressure and f_i are external body forces (e.g. buoyancy forces). Equation (3) is an exemplary transport equation for a scalar quantity s, which might be incorporated into the problem (e.g. for temperature or concentrations of species), and α and g denote the corresponding diffusion coefficient and source term, respectively. For the sake of simplicity, we assume that μ, α and ρ are constant.

The equation system (1)–(3) with the unknowns u_i, p, and s has to be completed by suitable (problem-dependent) boundary conditions, which we will not discuss here (see e.g. Reference [13] for the various possibilities and Section 5 for examples).

For our purpose, i.e. employing a spectral discretization technique to the above transport equations, it is more convenient to consider them in a non-conservative form. Under the above assumptions, Equations (2) and (3) can be rewritten in the form

$$\rho\frac{\partial u_i}{\partial t} - \nu\frac{\partial^2 u_i}{\partial x_j^2} + \rho u_j\frac{\partial u_i}{\partial x_j} = -\frac{\partial p}{\partial x_i} + \rho f_i \tag{4}$$

$$\rho\frac{\partial s}{\partial t} - \alpha\frac{\partial^2 s}{\partial x_j^2} + \rho u_j\frac{\partial s}{\partial x_j} = \rho g \tag{5}$$

Equations (4) and (5) have the form of the following general scalar transport equation:

$$\rho \frac{\partial \phi}{\partial t} - \Gamma \frac{\partial^2 \phi}{\partial x_j^2} + \Lambda_j \frac{\partial \phi}{\partial x_j} = f \tag{6}$$

where ϕ represents either u_i or s and the coefficients Γ and Λ_j and the source term f take the specific form to resemble Equations (4) and (5). In the following, without loss of generality, we can thus focus our considerations on Equation (6). Furthermore, we assume orthogonal problem domains, which are mapped onto the unit cube $[-1,1]^3$. A generalization to non-orthogonal domains, which can be mapped to the unit cube, poses no principal problems. However, to focus on the implicit treatment and the multi-domain technique, we will not discuss this issue here.

2.2. *Spectral discretization of scalar transport equation*

The basic principles of the employed spectral discretization procedure are outlined in detail in Reference [14], so only a brief summary is given here. The method is based on the use of Chebyshev polynomials as ansatz functions, with which an arbitrary function ϕ defined in the unit cube $[-1,1]^3$ can be represented as

$$\phi(\mathbf{x}_{ijk}, t) \approx \sum_{l=0}^{N} \sum_{m=0}^{M} \sum_{n=0}^{K} a_{lmn}(t) T_l(x_{1i}) T_m(x_{2j}) T_n(x_{3k}) \tag{7}$$

where a_{lmn} are the unknown coefficients. The Chebyshev polynomials T_l, T_m and T_n are evaluated at the Gauss–Lobatto points

$$\mathbf{x}_{ijk} = (x_{1i}, x_{2j}, x_{3k}) = -\left(\cos\frac{i\pi}{N}, \cos\frac{j\pi}{M}, \cos\frac{k\pi}{K}\right) \tag{8}$$

for $i = 0,\ldots,N,\ j = 0,\ldots,M,$ and $k = 0,\ldots,K$.

For the temporal discretization of the time derivative in Equation (6) a second-order implicit scheme (backward differencing formula) is employed [15]:

$$\frac{\partial \phi}{\partial t} \approx \frac{3\phi^{n+1} - 4\phi^n + \phi^{n-1}}{2\Delta t} \tag{9}$$

where Δt is the time-step size and the superscript n denotes the time level t_n (for ease of notation we restrict ourselves to equidistant time steps; a generalization to variable time-step sizes is straightforward). Λ_j and f in Equation (6), which in general may be time dependent, are evaluated (explicitly) by

$$\Lambda_j^{n+1} = 2\Lambda_j^n - \Lambda_j^{n-1} \quad \text{and} \quad f^{n+1} = 2f^n - f^{n-1} \tag{10}$$

which preserves the second-order temporal accuracy of the scheme. We remark that for initiating the two-level scheme the first time step is performed by the (one-level) backward Euler scheme.

The spatial derivatives are approximated (implicitly) using Lagrange polynomials at time level t_{n+1} by

$$\frac{\partial \phi}{\partial x_1}(\mathbf{x}_{ijk}, t_{n+1}) \approx \sum_{l=0}^{N} d_{il}^1 \phi_{ljk}^{n+1} \tag{11}$$

$$\frac{\partial^2 \phi}{\partial x_1^2}(\mathbf{x}_{ijk}, t_{n+1}) \approx \sum_{l=0}^{N} d_{il}^2 \phi_{ljk}^{n+1} \tag{12}$$

where d_{il}^1 and d_{il}^2 denote the coefficients of the spatial differentiation matrices with respect to x_1 (see e.g. Reference [14]). Similar definitions apply to the directions x_2 and x_3. ϕ_{ljk}^{n+1} denotes the value of ϕ at $\mathbf{x}_{ljk}$.

In summary, the above discretization procedure gives rise to an approximation of Equation (6) of the following general form:

$$\begin{aligned} &\sigma \phi_{ijk}^{n+1} + \Gamma(A_{il}^2 \phi_{ljk}^{n+1} + B_{jm}^2 \phi_{imk}^{n+1} + C_{kn}^2 \phi_{ijn}^{n+1}) \\ &\quad + \Lambda_1 A_{il}^1 \phi_{ljk}^{n+1} + \Lambda_2 B_{jm}^1 \phi_{imk}^{n+1} + \Lambda_3 C_{kn}^1 \phi_{ijn}^{n+1} = F_{ijk} \end{aligned} \tag{13}$$

with matrices $\mathbf{A}^1, \mathbf{B}^1, \mathbf{C}^1$ and $\mathbf{A}^2, \mathbf{B}^2, \mathbf{C}^2$ composed of the derivative operators for the first and second spatial derivatives, respectively. These matrices also include the boundary conditions (of Dirichlet or Neumann type). We emphasize that Λ_j, representing the convection coefficients, can depend on location and time (however, for simplicity, we suppress the corresponding indices). The term F_{ijk} comprises known quantities, i.e. source terms and terms resulting from boundary conditions, and σ is a scalar. An explicit analogon of the above discretization is formulated in References [16, 17]. In Section 5 a comparison of the explicit and implicit methods will be given.

2.3. *Pressure–correction scheme*

For the coupling velocity and pressure, a pressure–correction scheme employing a predictor–corrector technique is used. An explicit version of the scheme is discussed in detail in Reference [17], so we only recall here the basic steps distinguishing the explicit and implicit treatments of the convective terms. For ease of presentation, we write the algorithm for the spatially continuous equations. The global iteration process is as follows:

1. Initialize the field values u_i, p, s with some initial values.
2. Predict the (provisional) pressure $\tilde{p}^{n+1}$ from the Navier–Stokes and continuity equations with according boundary conditions (see Reference [17]):

$$\frac{\partial^2 \tilde{p}^{n+1}}{\partial x_j^2} = F^{n+1} \tag{14}$$

with

$$F^{n+1} = -\frac{\partial}{\partial x_i}\left[2\rho\left(u_j \frac{\partial u_i}{\partial x_j} - f_i\right)^n - \rho\left(u_j \frac{\partial u_i}{\partial x_j} - f_i\right)^{n-1}\right] \tag{15}$$

3. Solve the momentum equations for the (provisional) velocity components $\tilde{u}_i^{n+1}$:
   (a) explicit formulation

$$\mu \frac{\partial^2 \tilde{u}_i^{n+1}}{\partial x_j^2} - \rho \frac{3\tilde{u}_i^{n+1}}{2\Delta t} = F_i^{n+1} \tag{16}$$

with

$$F_i^{n+1} = \frac{\partial \tilde{p}^{n+1}}{\partial x_i} + 2\rho \left(u_j \frac{\partial u_i}{\partial x_j} - f_i \right)^n - \rho \left(u_j \frac{\partial u_i}{\partial x_j} - f_i \right)^{n-1} - \rho \frac{4u_i^n - u_i^{n-1}}{2\Delta t} \tag{17}$$

   (b) implicit formulation

$$\mu \frac{\partial^2 \tilde{u}_i^{n+1}}{\partial x_j^2} - \rho(2u_j^n - u_j^{n-1}) \frac{\partial \tilde{u}_i^{n+1}}{\partial x_j} - \rho \frac{3\tilde{u}_i^{n+1}}{2\Delta t} = F_i^{n+1} \tag{18}$$

with

$$F_i^{n+1} = \frac{\partial \tilde{p}^{n+1}}{\partial x_i} - 2\rho f_i^n + \rho f_i^{n-1} - \rho \frac{4u_i^n - u_i^{n-1}}{2\Delta t} \tag{19}$$

4. Solve the pressure–correction equation with homogeneous Neumann boundary conditions for the pressure–correction $\psi^n = p^{n+1} - \tilde{p}^{n+1}$:

$$\frac{\partial^2 \psi^n}{\partial x_j^2} = \frac{3\rho}{2\Delta t} \frac{\partial \tilde{u}_j^{n+1}}{\partial x_j} \tag{20}$$

5. Correct velocities and calculate pressure:

$$u_i^{n+1} = \tilde{u}_i^{n+1} - \frac{2\Delta t}{3\rho} \frac{\partial \psi^n}{\partial x_i} \tag{21}$$

$$p^{n+1} = \tilde{p}^{n+1} + \psi^n \tag{22}$$

6. Solve the scalar transport equation (if involved) for s^{n+1}:
   (a) explicit formulation

$$\alpha \frac{\partial^2 s^{n+1}}{\partial x_j^2} - \rho \frac{3s^{n+1}}{2\Delta t} = F^{n+1} \tag{23}$$

with

$$F^{n+1} = 2\rho \left(u_j^{n+1} \frac{\partial s^n}{\partial x_j} - g^n \right) - \rho \left(u_j^{n+1} \frac{\partial s^{n-1}}{\partial x_j} - g^{n-1} \right) - \rho \frac{4s^n - s^{n-1}}{2\Delta t} \tag{24}$$

   (b) implicit formulation

$$\alpha \frac{\partial^2 s^{n+1}}{\partial x_j^2} - \rho u_j^{n+1} \frac{\partial s^{n+1}}{\partial x_j} - \rho \frac{3s^{n+1}}{2\Delta t} = F^{n+1} \tag{25}$$

with

$$F^{n+1} = -2\rho g^n + \rho g^{n-1} - \rho \frac{4s^n - s^{n-1}}{2\Delta t} \tag{26}$$

7. Return to step 2 and calculate the next time step or stop, if last time step.

One iteration of the above pressure–correction scheme requires the solution of several systems of linear equations (in steps 2, 3, 4 and 6). It can be seen that all these systems, i.e. Equations (14), (16) or (18), (20), (23) or (25), have the form of Equation (13). For all systems the same solution method, which will be outlined in the next section, can be employed.

Linear systems (14) and (20) for the pressure and the pressure correction usually correspond to discrete Poisson equations with Neumann boundary conditions (except in case of prescribed pressure boundary conditions, see e.g. Reference [13]). Thus, the solutions of these systems are uniquely determined only up to an additive constant (the dimension of the kernel of the system matrix is 1). To fix the corresponding additional degree of freedom, we follow a proposal given in Reference [18] considering an extended system with an additional unknown λ:

$$\left[\begin{array}{c|c} & 1 \\ \mathbf{A} & \vdots \\ & 1 \\ \hline 1 \quad \cdots \quad 1 & 0 \end{array}\right] \left[\begin{array}{c} \boldsymbol{\Phi} \\ \hline \lambda \end{array}\right] = \left[\begin{array}{c} \mathbf{F} \\ \hline \omega \end{array}\right] \tag{27}$$

where ω is a scalar that can be chosen arbitrarily and $\mathbf{A}\boldsymbol{\Phi} = \mathbf{F}$ denotes the original system.

3. LINEAR SYSTEM SOLVER

From the numerical efficiency point of view, the solution of the linear systems arising during the pressure–correction scheme is one of the key issues. For the case of an explicit treatment of convective terms in Reference [1], a direct solver is introduced which has turned out to work very efficiently. However, in the general case such a direct solver cannot be applied in an economic way because the corresponding system matrices vary during the pressure–correction iterations. Here, the use of an iterative linear system solver is superior with respect to computational efficiency. The iterative solver employed makes use of the ideas of the direct solver by using a variant of it as a preconditioner within a Krylov subspace method. In the following, the various components of the iterative solver, which closely follows ideas developed in References [3–5], are described.

3.1. Preconditioned restarted GMRES method

Let us denote system (13) to be solved in symbolic form by

$$\mathbf{A}\boldsymbol{\Phi} = \mathbf{F} \tag{28}$$

With a suitable (non-singular) preconditioning matrix $\mathbf{Q}$, which we will specify later on, system (28) can be written equivalently in the form

$$\underbrace{\mathbf{Q}^{-1}\mathbf{A}}_{\tilde{\mathbf{A}}}\boldsymbol{\Phi} = \underbrace{\mathbf{Q}^{-1}\mathbf{F}}_{\tilde{\mathbf{F}}} \tag{29}$$

For the solution of the preconditioned system $\tilde{\mathbf{A}}\boldsymbol{\Phi} = \tilde{\mathbf{F}}$, the GMRES method proposed by Saad and Schultz [19], which belongs to the most efficient solvers for non-symmetric systems, is employed. The method has a limited memory requirement and usually shows a good convergence rate even for ill-conditioned system matrices.

Starting from an initial guess $\boldsymbol{\Phi}_0$ for $k = 1, 2, \ldots$ the GMRES method constructs an approximation to the linear system solution of the form

$$\boldsymbol{\Phi}_k = \boldsymbol{\Phi}_0 + \boldsymbol{\delta}_k \tag{30}$$

where $\boldsymbol{\delta}_k$ is sought in the k-dimensional (Krylov) subspace

$$\mathscr{S}^k = \{\mathbf{r}_0, \tilde{\mathbf{A}}\mathbf{r}_0, \tilde{\mathbf{A}}^2\mathbf{r}_0, \ldots \tilde{\mathbf{A}}^{k-1}\mathbf{r}_0\} \tag{31}$$

with $\mathbf{r}_0 = \tilde{\mathbf{F}} - \tilde{\mathbf{A}}\boldsymbol{\Phi}_0$ denoting the initial residual. Hereby, $\boldsymbol{\Phi}_k$ is determined such that the Euclidean norm of the corresponding residual $\mathbf{r}_k$ takes a global minimum.

The restarted form of GMRES, denoted by GMRES(k), which uses a relatively small subspace size k (compared with the dimension of the system matrix), evaluates $\boldsymbol{\Phi}_k$, which is then used as a new starting value $\boldsymbol{\Phi}_0$. This process is repeated until the converged solution is obtained (in our computations we employ the criterion that the norm of the residual is less than $\varepsilon = 10^{-15}$). The larger the value of k is taken, the better the convergence and robustness properties of the procedure. However, with increasing k the memory requirement also increases (linearly with k), such that a reasonable compromise has to be found. In all our computations GMRES(40) is employed. Compared with corresponding applications of the method to systems resulting from finite-volume or finite-element discretizations, the value $k = 40$ is relatively large. However, it can usually be employed without creating memory problems when using spectral methods due to the low system dimension.

With respect to implementation efficiency, it is important to note that the preconditioned GMRES(k) method does not require the coefficient matrix $\mathbf{A}$ and the preconditioning matrix $\mathbf{Q}$ to be constructed explicitly in matrix form. This is because only the results of matrix–vector products $\mathbf{Y} = \mathbf{AX}$ and the solutions of systems $\mathbf{QY} = \mathbf{X}$ are needed. When evaluating the matrix–vector products with $\mathbf{A}$ or solving the systems with $\mathbf{Q}$, the special form of Equation (13) can be exploited in order to minimize the computational effort. A detailed explanation of the corresponding implementation of the restarted GMRES method can be found in Reference [20].

3.2. *Preconditioner*

The preconditioner employed is based on the fast direct solver developed in Reference [1] for systems of the type of Equation (13), with $\Gamma = \bar{\Gamma} = \text{const.}$ and $\Lambda_j = 0$ (resulting with an explicit treatment of convective terms), i.e.

$$\sigma\Phi_{ijk} + \bar{\Gamma}(A^2_{il}\Phi_{ljk} + B^2_{jm}\Phi_{imk} + C^2_{kn}\Phi_{ijn}) = \bar{F}_{ijk} \tag{32}$$

where $\bar{F}_{ijk}$ differs from F_{ijk} in Equation (13), since it additionally includes the (explicitly treated) convective terms. We briefly recall the corresponding algorithm because the preconditioner employed will closely follow the underlying procedure.

The direct solver is based on a diagonalization of the matrices $\mathbf{A}^2$, $\mathbf{B}^2$, and $\mathbf{C}^2$ in Equation (32), which can be performed in a preprocessing stage:

$$D^{x_1}_{ps} = P_{pi} A^2_{il} P^{-1}_{ls}$$

$$D^{x_2}_{qs} = Q_{qj} B^2_{jm} Q^{-1}_{ms}$$

$$D^{x_3}_{rs} = R_{rk} C^2_{kn} R^{-1}_{ns}$$

The inverse matrices of $\mathbf{P}$, $\mathbf{Q}$, and $\mathbf{R}$ are composed (columnwise) of the eigenvectors of $\mathbf{A}^2$, $\mathbf{B}^2$, and $\mathbf{C}^2$, respectively. The entries of the diagonal matrices $\mathbf{D}^1$, $\mathbf{D}^2$, and $\mathbf{D}^3$ correspond to the eigenvalues α_p, β_q, and γ_r of $\mathbf{A}^2$, $\mathbf{B}^2$ and $\mathbf{C}^2$, respectively. Equation (32) can thus be written as

$$\sigma \Phi^*_{ijk} + \bar{\Gamma}(A^2_{il}\Phi^*_{ljk} + B^2_{jm}\Phi^*_{imk} + C^2_{kn}\Phi^*_{ijn}) = \bar{F}^*_{ijk} \tag{33}$$

or

$$\Phi^*_{pqr} = \frac{F^*_{pqr}}{\sigma + \bar{\Gamma}(\alpha_p + \beta_q + \gamma_r)} \tag{34}$$

with the matrices

$$\Phi^*_{pqr} = \Phi_{ijk} P_{pi} Q_{qj} R_{rk} \quad \text{and} \quad F^*_{pqr} = F_{ijk} P_{pi} Q_{qj} R_{rk} \tag{35}$$

According to the above relations, the solution of linear system (32) can efficiently be obtained via the following steps:

- Preprocessing: Computation of eigenvalues and eigenvectors of $\mathbf{A}^2$, $\mathbf{B}^2$, $\mathbf{C}^2$.
- *Step* 1: Computation of $F^*_{pqr} = F_{ijk} P_{pi} Q_{qj} R_{rk}$.
- *Step* 2: Computation of $\Phi^*_{pqr} = F^*_{pqr}/[\sigma + \bar{\Gamma}(\alpha_p + \beta_q + \gamma_r)]$.
- *Step* 3: Computation of $\Phi_{ijk} = \Phi^*_{pqr} P^{-1}_{ip} Q^{-1}_{jq} R^{-1}_{kr}$.

The efficiency of the method within a pressure–correction scheme as outlined in Section 2.3 is mainly due to the fact that the above diagonalization has to be done only once in a preprocessing step, since the matrices $\mathbf{A}^2$, $\mathbf{B}^2$ and $\mathbf{C}^2$ do not change during the pressure–correction iterations. In the general case of Equation (13), this is no longer true. Thus, the diagonalization would be necessary in each iteration, making the usage of the method inefficient. However, when used as a preconditioner within an outer iterative solver, the basic ideas of the procedure can be kept.

The preconditioning matrix $\mathbf{Q}$, which should be an approximation of $\mathbf{A}$, is chosen to correspond to a reduced form of Equation (13) similar to Equation (32). We obtain a simple approximation if we neglect the convective parts, i.e. $\Lambda_j = 0$, and use a mean value for the diffusion coefficient Γ:

$$\bar{\Gamma} = \frac{1}{2}\left[\max_{i,j,k}\{\Gamma(\mathbf{x}_{ijk})\} + \min_{i,j,k}\{\Gamma(\mathbf{x}_{ijk})\}\right] \tag{36}$$

This implies that only the diffusive terms are used for the preconditioning, which yield satisfactory convergence rates for diffusion-dominated problems. For a more elaborate preconditioning, also the matrices $\mathbf{A}^1$, $\mathbf{B}^1$ and $\mathbf{C}^1$ can be included into the preconditioning matrix $\mathbf{Q}$, e.g. by

using averaged values for Λ_j defined in analogy to Equation (36). This gives rise to a well-performing preconditioner also for convection-dominated problems. However, for our computations reported in Section 5, the preconditioning based only on the diffusive terms is employed.

We remark that for the pressure-related linear systems (14) and (20), since there are no convective terms, the above preconditioner in the mono-domain case yields the exact solution, such that actually no GMRES iteration is needed (this is no longer true for the multi-domain case; see next section).

4. EXTENSION TO MULTIPLE DOMAINS

The considerations so far were limited to simple (mono-block) domains that can be mapped onto the unit cube. In this section, we describe how the method can be extended to moderate complex geometries requiring a multi-block environment for modelling. The corresponding multi-domain approach employed is due to Bramble *et al.* [10–12]. In Reference [21] this technique has been used as a preconditioner for a conjugate gradient method in a finite-element setting.

Again, without loss of generality, we describe the technique for the scalar transport equation (6) only. Its application to flow problems is then straightforward via the pressure–correction scheme, just as for the mono-domain case.

4.1. Domain decomposition technique

For ease of presentation, we restrict ourselves in the following to a partitioning of a square (two-dimensional) domain into four sub-domains (see Figure 1), which is sufficient to illustrate the basic properties of the method. The extensions to more sub-domains and three-dimensional cases are straightforward.

We have to distinguish three different categories of grid points and corresponding entries in the discrete system:

- The internal points $\mathbf{\Phi}_i$ within each sub-domain Ω_i $(i=1,\ldots,4)$ with corresponding system matrices $\mathbf{A}_i$ and source vectors $\mathbf{F}_i$.
- The points $\mathbf{\Phi}_{12}$, $\mathbf{\Phi}_{13}$, $\mathbf{\Phi}_{24}$, $\mathbf{\Phi}_{34}$ along the interfaces Γ_{12}, Γ_{13}, Γ_{24}, Γ_{34} with corresponding system matrices $\mathbf{A}_{12}$, $\mathbf{A}_{13}$, $\mathbf{A}_{24}$, $\mathbf{A}_{34}$ and source vectors $\mathbf{F}_{12}$, $\mathbf{F}_{13}$, $\mathbf{F}_{24}$, $\mathbf{F}_{34}$.
- The vertex points ϕ_{1234} (only *one* in our example) with corresponding system matrix entry A_{1234} and source vector entry F_{1234}.

With a corresponding numbering of the unknowns (first the vertex points, then the interface points, finally the internal points) this gives rise to a partitioned discrete system having the following structure:

$$\left[\begin{array}{c|cccc|cccc} A_{1234} & * & * & * & * & & & & \\ \hline * & \mathbf{A}_{12} & & & & * & * & & \\ * & & \mathbf{A}_{13} & & & * & & * & \\ * & & & \mathbf{A}_{24} & & & * & & * \\ * & & & & \mathbf{A}_{34} & & & * & * \\ \hline & * & * & & & \mathbf{A}_1 & & & \\ & * & & * & & & \mathbf{A}_2 & & \\ & & * & & * & & & \mathbf{A}_3 & \\ & & & * & * & & & & \mathbf{A}_4 \end{array}\right] \left[\begin{array}{c} \phi_{1234} \\ \hline \mathbf{\Phi}_{12} \\ \mathbf{\Phi}_{13} \\ \mathbf{\Phi}_{24} \\ \mathbf{\Phi}_{34} \\ \hline \mathbf{\Phi}_1 \\ \mathbf{\Phi}_2 \\ \mathbf{\Phi}_3 \\ \mathbf{\Phi}_4 \end{array}\right] = \left[\begin{array}{c} F_{1234} \\ \hline \mathbf{F}_{12} \\ \mathbf{F}_{13} \\ \mathbf{F}_{24} \\ \mathbf{F}_{34} \\ \hline \mathbf{F}_1 \\ \mathbf{F}_2 \\ \mathbf{F}_3 \\ \mathbf{F}_4 \end{array}\right] \tag{37}$$

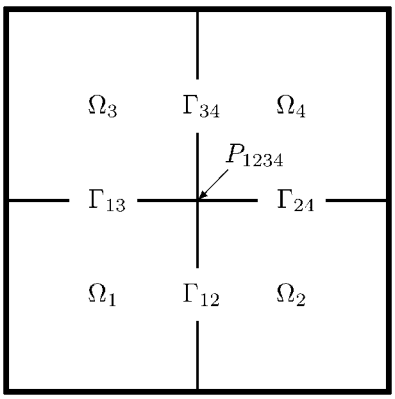

Figure 1. Decomposition of problem domain Ω into sub-domains Ω_1, Ω_2, Ω_3, Ω_4 with interfaces Γ_{12}, Γ_{13}, Γ_{24}, Γ_{34} and vertex point P_{1234}.

The symbol $*$ indicates system matrix entries which are due to a coupling between points of different categories. The corresponding coupling conditions will be discussed in the next section.

For the solution of system (37) the preconditioned restarted GMRES method is applied to the full system. For the preconditioning a variety of more or less elaborate strategies for the approximation of the system matrix in Equation (37) are possible. We propose here a rather simple approach:

- The entries $\mathbf{A}_i$ corresponding to internal points are approximated by matrices $\mathbf{Q}_i$, each of which are derived in the same manner as described in Section 3.2 for the mono-domain case via the modified fast direct solver.
- The interface and vertex entries $\mathbf{A}_{12}$, $\mathbf{A}_{13}$, $\mathbf{A}_{24}$, $\mathbf{A}_{34}$ and A_{1234} are approximated by the corresponding diagonal entries $\mathbf{A}_{12}^{\mathrm{D}}$, $\mathbf{A}_{13}^{\mathrm{D}}$, $\mathbf{A}_{24}^{\mathrm{D}}$, $\mathbf{A}_{34}^{\mathrm{D}}$ and A_{1234}^{D} (e.g. $\mathbf{A}_{12}^{\mathrm{D}}$ denotes diag $\mathbf{A}_{12}$, etc.).
- The entries representing a coupling (symbol $*$) are neglected.

This yields a global preconditioning matrix of the form

$$\mathbf{Q} = \begin{bmatrix} A_{1234}^{\mathrm{D}} & & \\ & \mathbf{A}_{12}^{\mathrm{D}} \quad \mathbf{A}_{13}^{\mathrm{D}} \quad \mathbf{A}_{24}^{\mathrm{D}} \quad \mathbf{A}_{34}^{\mathrm{D}} & \\ & & \mathbf{Q}_1 \quad \mathbf{Q}_2 \quad \mathbf{Q}_3 \quad \mathbf{Q}_4 \end{bmatrix} \tag{38}$$

Due to its block-diagonal structure, the necessary solution of the system $\mathbf{QY} = \mathbf{X}$ can now be determined without much computational effort.

We remark that in the three-dimensional case there are four categories of points, i.e. internal ones, on area interfaces, on edges and vertices, that give rise to a 4×4 partitioning. Thus, the system structure becomes a bit more complicated, though the basic principles for the multi-domain treatment remain the same.

4.2. Interface conditions

Along the interfaces Γ_{12}, Γ_{13}, Γ_{24} and Γ_{34} we enforce the continuity of the solution and its first normal derivative. For instance, on Γ_{12} this leads to the conditions:

$$\phi|_{\Omega_1} = \phi|_{\Omega_2} \quad \text{and} \quad \left.\frac{\partial \phi}{\partial x_1}\right|_{\Omega_1} = \left.\frac{\partial \phi}{\partial x_1}\right|_{\Omega_2} \quad \text{on } \Gamma_{12} \tag{39}$$

For the vertex point P_{1234} the continuity of the solution and the first derivatives in all space directions x_i have to be enforced:

$$\begin{gathered} \phi|_{\Omega_1} = \phi|_{\Omega_2} = \phi|_{\Omega_3} = \phi|_{\Omega_4} \\ \left.\frac{\partial \phi}{\partial x_1}\right|_{\Gamma_{13}} = \left.\frac{\partial \phi}{\partial x_1}\right|_{\Gamma_{24}} \quad \text{and} \quad \left.\frac{\partial \phi}{\partial x_2}\right|_{\Gamma_{12}} = \left.\frac{\partial \phi}{\partial x_2}\right|_{\Gamma_{34}} \quad \text{in } P_{1234} \end{gathered} \tag{40}$$

Applying the spectral discretization to the above conditions gives the coupling entries in the discrete system. For instance, for the interface Γ_{12} from conditions (39) we obtain

$$\phi_{Nj}^{\Omega_1} = \phi_{0j}^{\Omega_2} \quad \text{and} \quad \sum_{l=0}^{N} d_{Nl}^1 \phi_{lj} = \sum_{l=0}^{N} d_{0l}^1 \phi_{lj} \tag{41}$$

for $j = 1, \ldots, M-1$. We have assumed here that the locations of grid points along interfaces of adjacent sub-domains coincide (matching grids). In principle, non-matching grids are also possible, requiring additional interpolations of function values and first derivatives. However, this will not be considered here.

Special care has to be taken for interface values located at a boundary, e.g. $\phi_{N0}^{\Omega_1}$ and $\phi_{00}^{\Omega_2}$. In the case of a Dirichlet boundary condition, an additional term in the source vector results, while for a Neumann boundary condition the corresponding values have to be expressed by the internal function values.

5. NUMERICAL RESULTS

Several test cases are considered to show the various features of the method and to investigate its performance. In particular, the following aspects are considered:

- performance and accuracy of the implicit treatment of convective terms as opposed to an explicit approach,
- spectral accuracy in comparison to other approaches,
- performance of the multi-domain approach with varying number of sub-domains and complexity of the problem geometry.

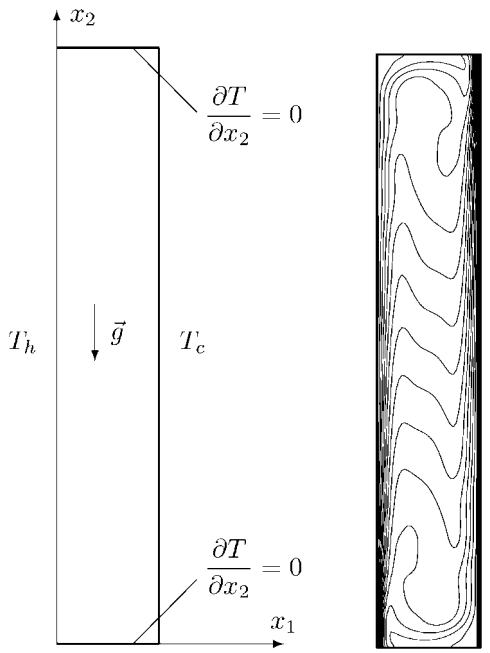

Figure 2. Problem configuration (left) and instantaneous isotherms (right) of buoyancy-driven flow in rectangular cavity with aspect ratio 1:8.

The basic investigations of the scheme is performed by means of two-dimensional test cases. This can be done without loss of generality, since the performance and accuracy issues hardly depend on the spatial dimension. Finally, an exemplary three-dimensional application is given.

For all steady-state computations a nested iteration technique is employed, where (linearly) extrapolated coarse grid results are used as starting values for fine grid iterations.

5.1. Buoyancy-driven flow in a rectangular cavity

Firstly, we will compare the performances of the explicit and implicit schemes for a time-dependent flow problem governed by the full set of (two-dimensional) equations (1)–(3) (with s representing the temperature). As a test case, we consider a buoyancy-driven flow in a rectangular cavity with aspect ratio 1:8, which was formulated in Reference [22] as a benchmark problem. In Figure 2, the problem configuration with temperature boundary conditions and a corresponding instantaneous temperature distribution are shown. For the velocity, no-slip conditions $u_1 = u_2 = 0$ on all cavity walls are employed. The Rayleigh number is $Ra = 10^5$ and the Prandtl number is $Pr = 0.71$. The time history of the Nusselt number at $x_1 = 0$ is indicated in Figure 3. After some irregular initial oscillations with very high amplitudes, the value of the Nusselt number regularly oscillates with constant amplitude and period.

The problem is computed with the explicit and implicit schemes for varying grid sizes and time-step sizes. For the evaluation of the accuracy the mean values $\overline{Nu}$, amplitudes a_{Nu},

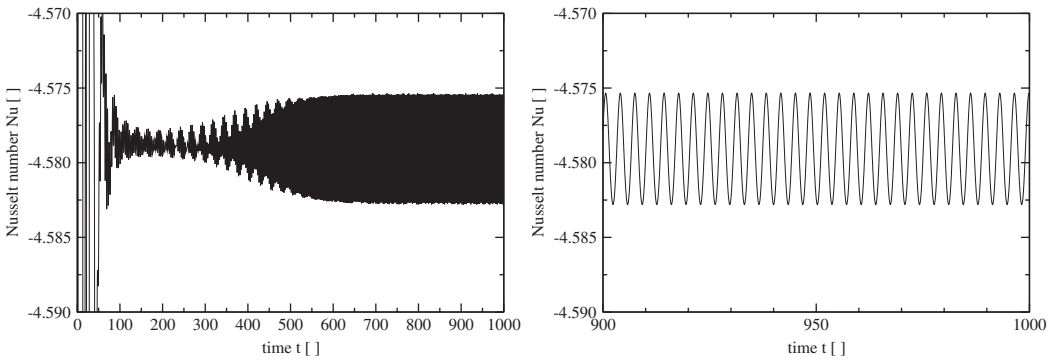

Figure 3. Time history of Nusselt number Nu at $x_1 = 0$ computed on 49×261 grid with $\Delta t = 0.025$ s for buoyancy-driven flow in rectangular cavity (left: time interval $[0, 1000]$; right: zoom to $[900, 1000]$).

Table I. Mean value, amplitude and period of Nusselt number at $x_1 = 0$ with different time step and grid sizes for buoyancy-driven flow in rectangular cavity.

Implicit	Grid 25×131			Grid 49×261		
Δt	$\overline{Nu}$	a_{Nu}	τ_{Nu}	$\overline{Nu}$	a_{Nu}	τ_{Nu}
0.1	−4.57662	± 0.00470	3.4304	−4.57678	± 0.00487	3.4291
0.05	−4.57852	± 0.00388	3.4231	−4.57880	± 0.00410	3.4218
0.025	−4.57890	± 0.00355	3.4241	−4.57918	± 0.00372	3.4223
0.0125	−4.57911	± 0.00346	3.4246	−4.57934	± 0.00365	3.4232
Explicit	Grid 25×131			Grid 49×261		
Δt	$\overline{Nu}$	a_{Nu}	τ_{Nu}	$\overline{Nu}$	a_{Nu}	τ_{Nu}
0.0125	−4.57869	±0.00169	3.4301	—	—	—
0.00625	−4.57916	±0.00294	3.4272	—	—	—
0.003125	−4.57949	±0.00322	3.4264	−4.57936	±0.00327	3.4256

and periods τ_{Nu} of the Nusselt number (in the regularly oscillating state) are considered as reference values. The results are summarized in Table I. The implicit scheme provides a solution for all time-step sizes. Depending on the grid size, the explicit scheme is stable only for $\Delta t \leqslant 0.0125$ s (coarse grid) and $\Delta t \leqslant 0.003125$ s (fine grid). The reference values converge with a refinement in space and time to the same value. Evaluating the accuracy of the solutions, for a given time-step size the explicit scheme is always less accurate than the implicit scheme.

A comparison of the efficiency of the methods is presented in Table II, indicating the total CPU time and the averaged CPU time per time step for the various cases. As expected, the work per time step is higher for the implicit method, whereas the total computational work to obtain an accurate solution is distinctly lower. In summary, the superiority of the implicit scheme is clearly demonstrated.

Table II. CPU times (per time step and total until $t = 1000$ s) with different time step and grid sizes for buoyancy-driven flow in rectangular cavity (on Linux PC with PIII 1.1 GHz).

Implicit Δt	Grid 25×131		Grid 49×261	
	Time step (s)	Total (h)	Time step (s)	Total (h)
0.1	1.02	2.83	7.75	21.53
0.05	0.56	3.11	3.70	20.56
0.025	0.42	4.67	2.63	29.22
0.0125	0.36	8.02	2.51	55.68
Explicit Δt	Grid 25×131		Grid 49×261	
	Per time step (s)	Total (h)	Per time step (s)	Total (h)
0.1	Diverged		Diverged	
0.05	Diverged		Diverged	
0.025	Diverged		Diverged	
0.0125	0.18	4.07	Diverged	
0.00625	0.18	7.89	Diverged	
0.003125	0.18	15.7	1.71	152

In order to allow a comparison of the accuracy and efficiency of the present method to other approaches in Table III an evaluation of various results contributed to the benchmark computation defined in Reference [22] is given. Benchmark results are taken from References [23–27]. In the table the following information is indicated for the different computations: the spatial and temporal discretization methods employed, the computer employed with peak performance rate (in MFlops), the spatial and temporal resolutions, the total CPU times required normalized with the computer peak performance (CPU*Peak), the CPU times per degree of freedom and time step (CPU/dof-step), as well as average values, amplitudes, and periods of various benchmark quantities. The results illustrate that the present method shows a quite competitive performance in terms of accuracy and efficiency in comparison to other approaches. The accuracy can be best evaluated by comparing the amplitude values, which are the most critical ones, while the efficiency can be estimated from the CPU*Peak value.

5.2. *Taylor problem in L-shaped geometry*

For a first validation of the spectral accuracy of the multi-domain approach, we consider the well known Taylor problem in an L-shaped domain, for which the following analytical solution is available (see Reference [28]):

$$u_1(x_1, x_2) = -\cos(2\pi x)\sin(2\pi y)$$

$$u_2(x_1, x_2) = \sin(2\pi x)\cos(2\pi y)$$

$$p(x_1, x_2) = -(\cos(4\pi x) + \cos(4\pi y))/4$$

The problem configuration with the corresponding (coarsest) multi-domain grid is shown in Figure 4, where the contour lines of the u_1-velocity and the pressure p are also given.

Table III. Comparison of present method with various benchmark results for buoyancy-driven flow in rectangular cavity.

	Present	[23]	[24]	[25]	[26]	[27]
Space discretization	Chebyshev spectral	Galerk.—Legend. spectral	FE Q_1Q_0	FE Q_2Q_{-1}	FD 4th ord.	Chebyshev spectral
Time discretization	Implicit 2nd ord.	Explicit 2nd ord.	Explicit 2nd ord.	Implicit 2nd ord.	Explicit 4th ord.	Explicit 2nd ord.
Computer	AMD1100	NEC SX5	Alpha500	HP-J5000	Alpha500	NEC SX5
Peak MFlops	1100	8192	1000	1000	1000	8192
Grid size	49×261	40×160	81×401	105×481	96×768	48×180
Time step	0.025	0.001	0.002	≈ 0.14	0.0078	0.0017
CPU*Peak	1.2e8	5.6e8	2.0e8	2.2e9	1.2e9	1.2e8
CPU/dof-step	206 μs	10.8 μs	12.11 μs	6102 μs	12.31 μs	3 μs
			Nusselt number Nu at $x_1 = 0$			
Average	4.579183	4.57952	4.579	4.5821	4.567	4.57946
Amplitude	0.003717	0.003721	0.003360	0.00361	0.003565	0.003550
Period	3.4223	3.4068	3.446	3.4258	3.422	3.4115
			Velocity u_1 at point 1			
Average	0.056881	0.0566998	0.06112	0.05554	0.05616	0.056356
Amplitude	0.0288	0.0286217	0.02539	0.02774	0.02726	0.027415
Period	3.4218	3.4068	3.447	3.4259	3.422	3.4115
			Velocity u_2 at point 1			
Average	0.4615	0.461864	0.4638	0.46074	0.4605	0.46188
Amplitude	0.0406	0.040017	0.03630	0.03900	0.03859	0.038603
Period	3.4218	3.4068	3.446	3.4259	3.422	3.4115
			Temperature T at point 1			
Average	0.265580	0.265460	0.2663	0.26468	0.2647	0.26548
Amplitude	0.022658	0.022368	0.01985	0.02158	0.02134	0.0213675
Period	3.4218	3.4068	3.447	3.4259	3.422	3.4115

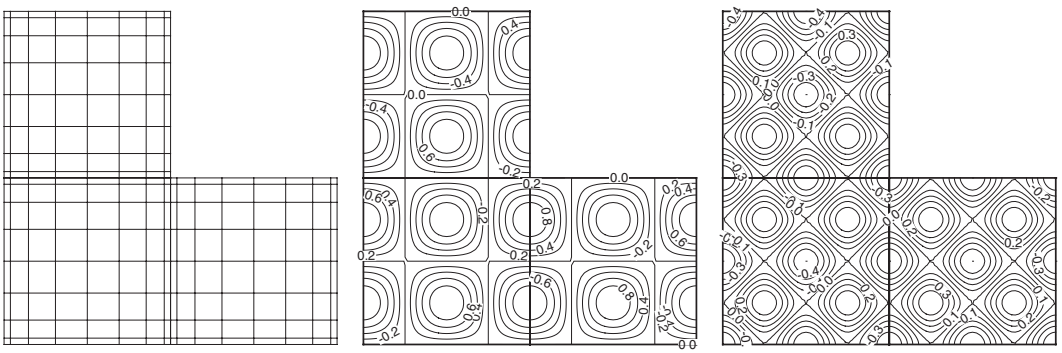

Figure 4. Problem domain with multi-domain grid (left) and contour lines for u_1-velocity (middle) and pressure (right) for Taylor problem in L-shaped geometry.

Table IV. Errors for velocity and pressure in maximum norm $\|\cdot\|_\infty$ with varying grid size for L-shaped Taylor problem.

Sub-domain grid	$\|u - u_h\|_\infty$	$\|p - p_h\|_\infty$
9×9	1.7E-3	1.0E-1
17×17	1.6E-8	4.2E-6
33×33	3.7E-15	7.1E-13
65×65	2.6E-15	1.1E-14

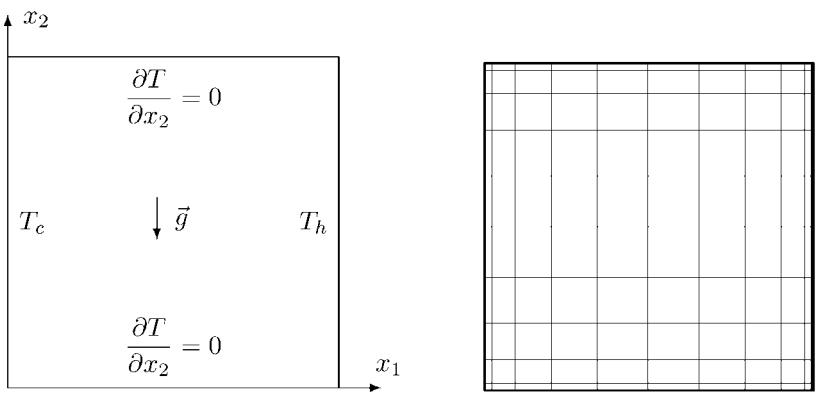

Figure 5. Problem configuration of buoyancy-driven flow in square cavity (left) and (mono-domain) grid with 11×11 points (right).

The computations are carried out with a time-step size of $\Delta t = 10^{-4}$ s, leading for all grids to a stable behaviour. Starting with the analytical solution as an initial condition, 100 iterations have been performed. In Table IV the errors (to the analytical solution) for the absolute velocity and the pressure in the maximum norm $\|\cdot\|_\infty$ are given when computing the solution with our multi-domain spectral method for varying grid size. The results clearly show that the multi-domain method also features a spectral accuracy. For the third grid, the solutions already reach the precision of the roundoff error.

5.3. *Buoyancy-driven flow in a square cavity*

For a detailed investigation of various aspects of the spectral scheme, we consider next the steady buoyancy-driven flow in a square cavity. The problem configuration with temperature boundary conditions is shown in Figure 5 together with a corresponding 11×11 grid. For the velocity, we employ no-slip conditions $u_1 = u_2 = 0$ on all cavity walls. The problem parameters are chosen to yield a Rayleigh number of $Ra = 10^5$ and a Prandtl number of $Pr = 0.71$.

We investigate the multi-domain approach with respect to its accuracy and its dependence on the number and the shape of the sub-domains. For this purpose, besides the mono-domain grid (see Figure 5) we consider various multi-domain grid systems with 4, 9 and 16 uniform blocks as well as with four non-uniform blocks (see Figure 6, where for each case the coarsest grid is shown). The corresponding performance results of the spectral scheme can be seen from Figures 7–9 showing the error in the Nusselt number versus the number of grid points,

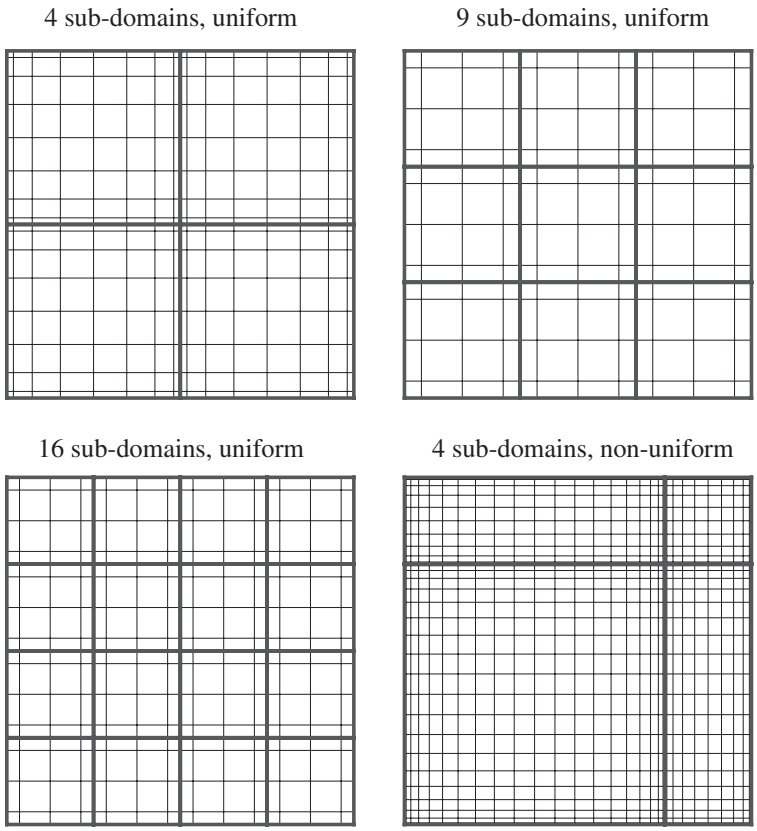

Figure 6. Multi-domain grid systems (coarsest grids) for buoyancy-driven square cavity problem.

the CPU time versus the number of grid points, and the error in the Nusselt number versus the CPU time, respectively, for the various grid systems. The reference value for calculating the error is the solution obtained on a 321×321 grid ($Nu = 4.5216362$). For comparison, results for a finite-volume scheme are also given. The latter are obtained with the code FASTEST [29], which employs a second-order finite-volume discretization on block-structured grids, a pressure–correction scheme of SIMPLE type for coupling of velocity and pressure, and a full multigrid algorithm for convergence acceleration. It can therefore be considered as an efficient representative of this class of methods (see e.g. References [30, 31]).

A variety of conclusions can be drawn from the results:

- The results clearly show the superiority of the spectral scheme (for all grid systems) compared with the finite-volume scheme with respect to accuracy. Of course, for a fixed number of grid points the finite-volume method is faster, such that there is a break-even point relating to the required accuracy, where the spectral scheme becomes more efficient.
- For a fixed number of grid points the spectral accuracy slightly deteriorates with increasing number of sub-domains, since the degree of the Chebyshev polynomials is determined

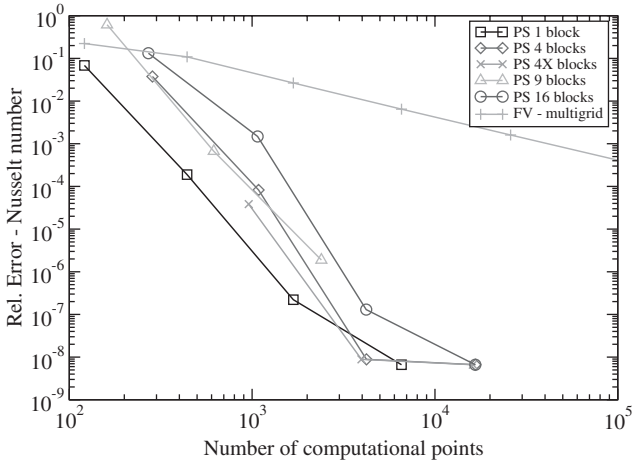

Figure 7. Error of Nusselt number versus number of grid points for various multi-domain grid systems for two-dimensional buoyancy-driven cavity problem.

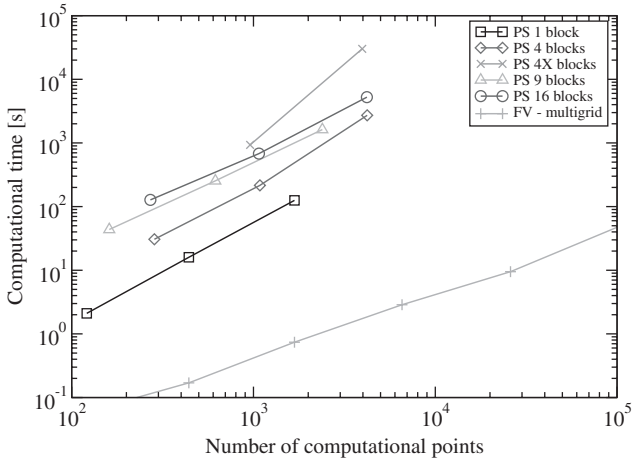

Figure 8. CPU time versus number of grid points for various multi-domain grid systems for buoyancy-driven square cavity problem (on Compaq AlphaServer ES40 677 MHz).

by the number of grid points in the sub-domains, which becomes smaller, if there are more sub-domains.

- For a fixed number of grid points in the sub-domains the accuracy hardly depends on the number of sub-domains. Also, the non-uniformity of the sub-domains has no significant effect on the accuracy.
- The CPU time increases with the number of sub-domains and with its non-uniformity.

To summarize, one can state that the multi-domain methodology principally preserves the spectral accuracy and, therefore, it appears to be well suited for problems actually requiring

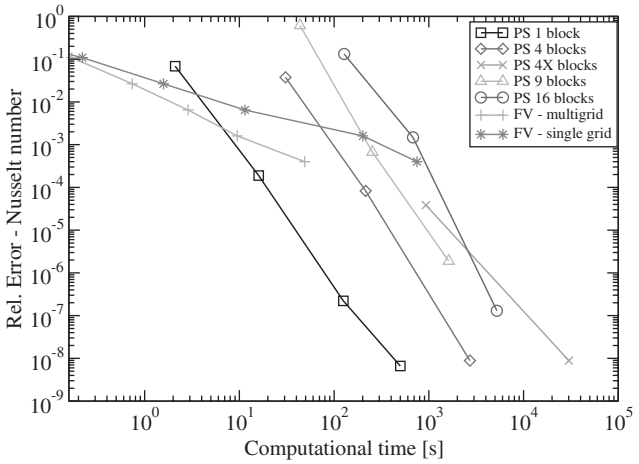

Figure 9. Error of Nusselt number versus CPU time for various multi-domain grid systems for buoyancy-driven square cavity problem (on Compaq AlphaServer ES40 677 MHz).

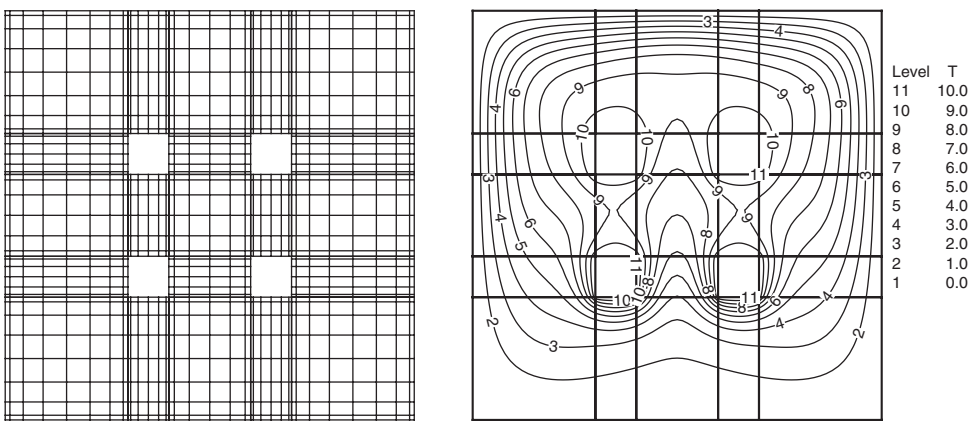

Figure 10. Heat exchanger configuration with multi-domain grid (left) and computed isotherms (right).

this feature. However, the number of sub-domains should be kept as small and as uniform as possible in order to retain a good ratio of accuracy and CPU time. With respect to parallelization on the basis of the multi-domain approach, it appears that the method will provide reasonable parallel efficiencies for moderate processor numbers, while it will not be efficient for massively parallel computations (which, however, will rarely be necessary, due to the high accuracy that can already be achieved with relatively small numbers of grid points).

5.4. Heat exchanger configuration

As a geometrically more complex example, we consider the buoyancy-driven flow in a two-dimensional heat exchanger configuration. The geometry is shown in Figure 10 together with the corresponding (coarsest) multi-domain grid and the computed isotherms. The square

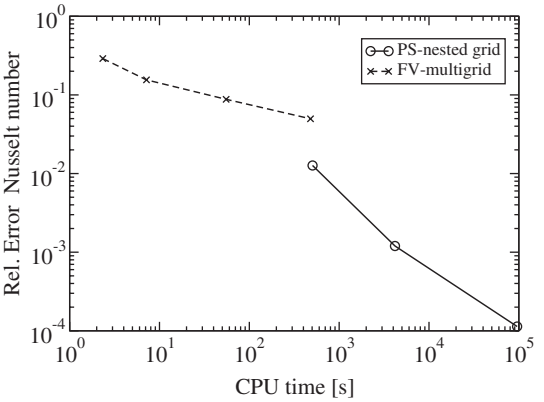

Figure 11. Relative error of Nusselt number versus CPU time for spectral and finite-volume methods for heat exchanger problem (on Compaq AlphaServer ES40 677 MHz).

obstacles have side lengths L and distances $2L$ from each other. The outer cavity has a side length $10L$. At the outer wall and at the square obstacles, low and high temperatures of $T = 1$ and 11 are prescribed, respectively. For the velocity, no-slip conditions $u_1 = u_2 = 0$ are assumed at all boundaries. The Rayleigh number based on the smallest distance between walls and obstacles (i.e. $3L$) is $Ra = 2700$ and the Prandtl number is $Pr = 0.71$.

In Figure 10(a) a comparison of the efficiency of the multi-domain spectral scheme to a block-structured finite-volume method (again realized with the multigrid code FASTEST) is given. For both approaches the relative errors in the Nusselt numbers compared to the CPU times (corresponding to varying grid size) are indicated. The Nusselt number is calculated by integrating over the sides of the obstacles. Again, the reference value for the Nusselt number corresponds to the value obtained on a very fine grid ($Nu = 1.76123$ with 82 304 grid points).

In addition, for this geometrically more complex case the significantly better performance of the spectral technique is clearly observed. With the finite-volume scheme on the finest grid with 47 424CVs, an accuracy of about 5×10^{-2} can be achieved in a CPU time of 500s, while with the spectral scheme already on the coarsest grid with 1013 grid points an accuracy of about 1×10^{-2} can be achieved within the same CPU time. To reach a corresponding accuracy with the finite-volume scheme a CPU time of around 10^5 s would be necessary. It should be mentioned that the finite-volume method suffers from calculating the Nusselt number with the first-order approximation of the derivatives at the boundary (Figure 11).

5.5. Three-dimensional buoyancy-driven cavity

In our last example, a three-dimensional computation with three non-periodic directions will be performed. The problem configuration consists of a cubical air-filled ($Pr = 0.71$) cavity with one pair of opposing faces ($x_1 = 0$ and L) at temperatures T_h and T_c, respectively (Figure 12). The four remaining faces are adiabatic. The Rayleigh number is chosen to be $Ra = 10^4$. The integral Nusselt number Nu at the face $x_1 = 0$ will serve as the reference value for evaluating the accuracy.

The problem is computed with one domain and with four sub-domains. In Table V the grid sizes used (per block) and the computed Nusselt numbers are indicated for both grid

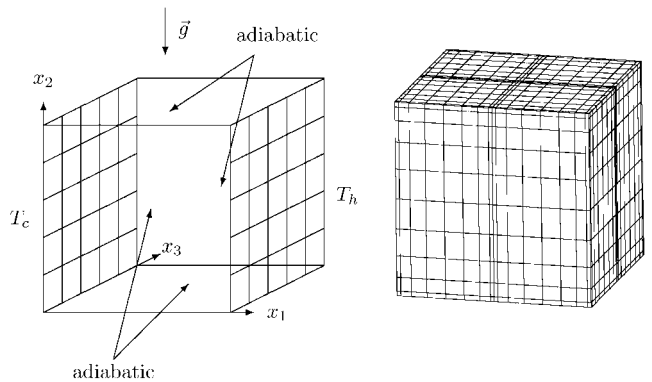

Figure 12. Problem configuration of buoyancy-driven flow in cube (left) and grid with four sub-domains with $9 \times 9 \times 11$ points each (right).

Table V. Nusselt numbers Nu at face $x_1 = 0$ computed with mono-domain and 4-domain grids with varying grid sizes for buoyancy driven flow in a cube.

	Grid size		Nusselt number Nu	
	Mono	4 Blocks	Mono	4 Blocks
Grid 1	$11 \times 11 \times 11$	$9 \times 9 \times 11$	2.051496	2.057104
Grid 2	$21 \times 21 \times 21$	$17 \times 17 \times 21$	2.055119	2.055097
Grid 3	$41 \times 41 \times 41$	$33 \times 33 \times 41$	2.055108	2.055108
Grid 4	$81 \times 81 \times 81$	—	2.055108	—
[32]	$81 \times 81 \times 81$		2.054	

systems with varying number of grid points. The reference value is taken from Tric *et al.* [32]. With grid refinement, the mono-domain and the multi-domain cases lead to the same Nusselt number, which is in close agreement with the reference value. For both grid systems the spectral accuracy is clearly observed.

6. CONCLUSIONS

We have presented an implicit pseudo-spectral method allowing for an efficient prediction of incompressible flows in moderately complex geometries. The method is based on a Chebyshev collocation discretization (in all three spatial dimensions) in a multi-domain setting in connection with an iterative solver, whose efficiency, in particular, is based on a preconditioner employing ideas from a direct Helmholtz solver.

It has been shown that due to its implicitness the approach features fairly good stability properties and that it is superior to corresponding explicit methods. The outstanding accuracy (with low numbers of grid points) due to the spectral type discretization has been demonstrated by comparisons with standard finite-volume techniques. These features are widely retained in the multi-domain case.

While we have focused our considerations on incompressible laminar flows with constant fluid parameters in orthogonal geometries, due to the inherent flexibility of the implicit spectral scheme, the applicability of the proposed solution procedure is not limited to such kind of problems. Extensions to non-orthogonal geometries or to other types of flow problems, i.e. turbulent flows described by the Reynolds-averaged Navier–Stokes equations with statistical turbulence modelling or compressible flows (at low-Mach number) with temperature-dependent density governed by the low-Mach number equations, are quite straightforward. These issues will be topics of forthcoming work.

ACKNOWLEDGEMENTS

The work was financed by the *Deutsche Forschungsgemeinschaft* (*DFG*) and the *Centre Nationale de la Recherche Scientifique* (*CNRS*) within the French-German research programme. *Numerical Flow Simulation*, the *CNRS network of CFD*, and the French-German PROCOPE programme. Furthermore, M. Schäfer was supported by CNRS as a visiting Associate Professor. All this support is gratefully acknowledged. Thanks are addressed to I. Raspo for valuable contributions to the work.

REFERENCES

1. Haldenwang P, Labrosse G, Abboudi S, Deville M. Chebyshev 3d spectral and 2d pseudo-spectral solvers for the Helmholtz equation. *Journal of Computational Physics* 1984; **55**:115–128.
2. Serre E, Crespo del Arco E, Bontoux P. Annular and spiral patterns in flows between rotating and stationary discs. *Journal of Fluid Mechanics* 2001; **434**:65–100.
3. Guillard H, Désidéri JA. Iterative methods with spectral preconditioning for elliplic equations. *Computational Methods in Applied Mechanics and Engineering* 1990; **80**:305–312.
4. Dimitropoulos CD, Edwards BJ, Chae K-S, Beris AN. Efficient pseudo-spectral flow simulations in moderately complex geometries. *Journal of Computational Physics* 1998; **144**:517–549.
5. Dimitropoulos CD. An efficient and robust spectral solver for nonseparable elliptic equations. *Journal of Computational Physics* 1997; **133**:186–191.
6. Macaraeg M, Streett CL. Improvements in spectral collocation through a multiple domain technique. *Applied Numerical Mathematics* 1986; **2**:95–108.
7. Lacroix JM, Peyret R, Pulicani JP. A spectral multidomain method for the Navier–Stokes equations with application to double diffusive convection. In *Proceedings of the 7th GAMM-Conference on Numerical Methods and Fluid Mechanics*, Deville M (ed.). Vieweg: Braunschweig, 1988; 164–174.
8. Raspo I, Ouazzani J, Peyret R. A spectral multidomain technique for the computation of the Czochralski melt configuration. *International Journal of Numerical Methods for Heat and Fluid Flow* 1996; **6**:31–58.
9. Raspo I. A direct spectral domain decomposition method for the computation of rotating flows in a T-shape geometry. *Computers and Fluids* 2002; **32**:431–456.
10. Bramble JH, Pasciak JE, Schatz AH. The construction of preconditioners for elliptic problems by substructuring I. *Mathematics of Computation* 1986; **47**:103–134.
11. Bramble JH, Pasciak JE, Schatz AH. The construction of preconditioners for elliptic problems by substructuring II. *Mathematics of Computation* 1987; **49**:1–16.
12. Bramble JH, Pasciak JE, Schatz AH. The construction of preconditioners for elliptic problems by substructuring III. *Mathematics of Computation* 1988; **51**:415–430.
13. Ferziger JH, Perić M. *Computational Methods for Fluid Dynamics*. Springer: Berlin, 1996.
14. Canuto C, Hussaini MY, Quateroni A, Zang TA. *Spectral Methods in Fluid Dynamics*. Springer: Berlin, 1988.
15. Vanel JM, Peyret R, Bontoux P. A pseudo-spectral solution of vorticity-streamfunction equations using the influence matrix technique. In *Numerical Methods in Fluid Mechanics*, Morton KW, Baines MJ (eds). Clarendon press: Oxford, 1986; 463–475.
16. Droll P, Schäfer M, Louchart O, Bontoux P. Coupling of a finite-volume method with a pseudo-spectral method. In *Computational Fluid Dynamics'98*. Wiley: Chichester, 1998; p. 1240–1245.
17. Hugues S, Randriamampianina A. An improved projection scheme applied to pseudo-spectral methods for the incompressible Navier–Stokes equations. *International Journal for Numerical Methods in Fluids* 1998; **28**: 501–521.
18. Hackbusch W. *Theorie und Numerik elliptischer Differentialgleichungen*. Teubner: Stuttgart, 1996.

19. Saad Y, Schultz MH. GMRES: a generalized minimal residual algorithm for solving nonsymmetric linear systems. *SIAM Journal on Scientific and Statistical Computing* 1986; **7**:856–869.
20. da Cunha RD, Hopkins TR. A parallel implementation of the restarted GMRES iterative method for nonsymmetric systems of linear equations. *Advances in Computer Mathematics* 1994; **2**(3):261–277.
21. De Valerio M, Schäfer M. Domain decomposition methods for the numerical solution of elliptic partial differential equations on array processors. In *Parallel Computing '91*. Elsevier: Amsterdam, 1992; 167–173.
22. Christon MA, Gresho PM, Sutton SB. Computational predictability of natural convection flows in enclosures. In *Proceedings of the First MIT Conference on Computational Fluid and Solid Mechanics*, Bathe KJ (ed.). Elsevier Science: Amsterdam, 2001.
23. Auteri F, Paroline N. Simulation of the differentially heated 8:1 rectangular cavity by a Galerkin–Legendre spectral projection method. In *Proceedings of the First MIT Conference on Computational Fluid and Solid Mechanics*. Bathe KJ (ed.). Elsevier Science: Amsterdam, 2001; 1451–1455.
24. Christon MA. LS-DYNA and the 8:1 differentially-heated cavity. In *Proceedings of the First MIT Conference on Computational Fluid and Solid Mechanics*, Bathe KJ (ed.). Elsevier Science: Amsterdam, 2001; 1460–1464.
25. Gresho PM, Sutton S. 8:1 Thermal cavity problem. In *Proceedings of the First MIT Conference on Computational Fluid and Solid Mechanics*, Bathe KJ (ed.). Elsevier Science: Amsterdam, 2001; 1482–1485.
26. Johnston H, Krasny R. Computational predictability of natural convection flows in enclosures: a benchmark problem. In *Proceedings of the First MIT Conference on Computational Fluid and Solid Mechanics*, Bathe KJ (ed.). Elsevier Science: Amsterdam, 2001; 1486–1489.
27. Xin S, Le Quéré P. An extended chebyshev pseudo-spectral contribution to the CPNCFE benchmark. In *Proceedings of the First MIT Conference on Computational Fluid and Solid Mechanics*, Bathe KJ (ed.). Elsevier Science: Amsterdam, 2001; 1509–1513.
28. Batchelor GK (ed.). *The Collected Work of G.I. Taylor*, vol. 2. Cambridge University Press: Cambridge, MA, 1960.
29. INVENT Computing GmbH. *FASTEST Manual*. Erlangen, 1999.
30. Durst F, Schäfer M. A parallel blockstructured multigrid method for the prediction of incompressible flows. *International Journal for Numerical Methods in Fluids* 1996; **22**:549–565.
31. Schäfer M, Turek S. Benchmark computations of laminar flow around a cylinder. In *Flow Simulation with High-Performance Computers II*, Hirschel EH (ed.). Notes on Numerical Fluid Mechanics, Vieweg: Braunschweig, 1996; 547–566.
32. Tric E, Betrouni M, Labrosse G. Accurate solutions of natural convection flow of air in a differentially heated cubic cavity. In *Computational Fluid Dynamics '98*. Wiley: Chichester, 1998; 979–982

